A Unique Distortion in $K_{1/3}Ba_{2/3}AgTe_2$: X-ray Diffraction Determination and Electronic Band Structure Analysis of Its Incommensurately Modulated Structure

O. Gourdon,[†] Jason Hanko,[‡] F. Boucher,[†] V. Petricek,[§] M.-H. Whangbo,[||] M. G. Kanatzidis,[‡] and M. Evain*[,†]

Laboratoire de Chimie des Solides, I.M.N., UMR C6502 CNRS, Université de Nantes, 2 rue de la Houssinière, BP 32229, 44322 Nantes Cedex 3, France, Department of Chemistry, Michigan State University and Center for Fundamental Materials Research, East Lansing, Michigan 48824, Institute of Physics, Academy of Sciences of the Czech Republic, Na Slovance 2, 180 40 Praha 8, Czech Republic, and Department of Chemistry, North Carolina State University, Raleigh, North Carolina 27695-8204

Received December 20, 1999

The incommensurately modulated structure of a square Te-net, namely that of $K_{1/3}Ba_{2/3}AgTe_2$, is determined from single-crystal X-ray diffraction data within a (3+1)D higher dimension formalism. The phase is shown to crystallize in the monoclinic symmetry, $P2_1(\alpha 0 \gamma)$ superspace group with the following lattice parameters: $a =$ 4.6441(10) Å, $b = 4.6292(12)$ Å, $c = 23.765(9)$ Å, and $\beta = 101.28(2)°$ with $\mathbf{q} = 0.3248(6)\mathbf{a}^* - 0.071(8)\mathbf{c}^*$, that is, in a symmetry different from that reported for the average structure (tetragonal) or that assumed from electron diffraction measurements (orthorhombic). After the introduction of a crenel function for the Te displacive description, the refinement converged to a residual factor $R = 0.033$ for 2583 observed reflections and 115 parameters ($R = 0.024$ and 0.101 for 1925 main reflections and 658 first-order satellites, respectively). The [Ag_2Te_2] and the Ba/K layers are found to be only weakly modulated. The modulation of the square Te-net is, however, both substantial and unique. Namely, it results in two different units: a "V"-shaped Te_3 trimer and a "W"-shaped Te_5 pentamer. To examine both unit types, which are segregated in domains that aperiodically alternate within the Te layers, first principles electronic band structure calculations were carried out for three model commensurate structures using the tight-binding linear-muffin-tin-orbital method (LMTO). The calculations show that the distorted structures of V-pattern (model 2) and W-pattern (model 3) are more stable than the average structure (model 1) and that the V-pattern distortion provides a slightly larger stabilization than does the W-pattern distortion. The Fermi surface calculated for the average structure shows nesting vectors that are consistent with the occurrence of the V- and W-pattern distortions in the Te layers. However, these vectors do not predict the observed modulation vector of the incommensurately distorted structure, because the stabilization energy associated with the distortion is not mainly dominated by the energy lowering of the occupied band levels near the Fermi level.

1. Introduction

Square nets of elements are common in many high-symmetry solid-state compounds. Examples include the Cu_2Sb structures,[1] the related ZrSiSe structures,[2] the PbO and anti-PbO structures,[3] the $ThCr_2Si_2$[4] structures, and some other less popular structure types.[5] In these structures, either a transition metal and/or a main group element form some kind of extended planar square net. The chemical, physical, and electronic properties of these compounds are largely decided by these square nets and by their interactions with the remaining part of the structure. Although hundreds of such structures have been reported to date, only a few are known for tellurium, e.g., the binary rare earth tellurides, $LnTe_2$, Ln_2Te_5, and $LnTe_3$,[6] $CsCe_3Te_8$[7] (defect net), $K_{0.33}Ba_{0.67}AgTe_2$,[8] and $KCuCeTe_4$.[9] Early investigations in $LnTe_3$ materials revealed numerous anomalies in their properties, now understood to arise from the Fermi surface driven charge density wave (CDW) distortion.

In all these cases, only an average Te-net structure has been determined by conventional X-ray crystallographic methods

* To whom correspondence should be addressed
[†] Université de Nantes.
[‡] Michigan State University and Center for Fundamental Materials Research.
[§] Academy of Sciences of the Czech Republic.
[||] North Carolina State University.

(1) Erlander, M.; Hägg, G.; Westgren, A. *Ark. Kemi. Min. Geol.* **1936**−**38**, *12B*, No. 1.
(2) Haneveld, A. J. K.; Jellinek, F. *Recl. Trav. Chim. Pays-Bas.* **1964**, *883*, 776−778.
(3) Byström, A. *Ark. Kemi. Min. Geol.* **1945**, *20A*, No. 11. (b) Grønvold, F.; Haraldsen, H.; Vihovde, *J. Acta Chem. Scand.* **1954,** *8*, 1927−1930.
(4) Ban, Z.; Sikirica, M. *Acta Crystallogr.* **1965**, *18*, 594−599.
(5) $LnNi_2Si_3$ (Ln = Sc, U): Kotur, B. Ya.; Bodak, O. I.; Gladyshevskii, E. I. *Sov. Phys; Kristallogr.* **1978**, *23* (1), 189−190. (b) $ScNiSi_3$: Kotur, B. Ya.; Bodak, O. I.; Mys'kiv, M. G.; Gladyshevskii, E. I. *Sov. Phys; Kristallogr.* **1977**, *22(2)*, 267−270. (c) $SmNiGe_3$: Bodak, O. I.; Pecharskii, V. K.; Mruz, O. Ya.; Zarodnik, V. Yu.; Vivits'ka, G. M.; Salamakha, P. S. *Dopov. Akad. Nauk. Ukr. RSR., Ser. B* **1985**, *2*, 36−38.
(6) Lin, W.; Steinfink, H.; Weiss, F. *J. Inorg. Chem.* **1965**, *4*, 877−881. (b) Wang, R.; Steinfink, H.; Bradley, W. F. *J. Inorg. Chem.* **1966**, *5*, 142−145. (c) Pardo, M.-P.; Flahaut, J.; Domange, L. C. R. *Bull. Soc. Chim. Fr.* **1964**, 3267−3271. (d) Ramsey T. H.; Steinfink, H.; Weiss, E. *J. Inorg. Chem.* **1965**, *4*, 1154−1157. (e) Norling, B. K.; Steinfink, H. *Inorg. Chem.* **1966**, *5*, 1488−1491.
(7) Patshke, R.; Heising, J.; Schindler, J.; Kannewurf, C. R.; Kanatzidis, M. G. *J. Solid State Chem.* **1998**, *135*, 111−115.
(8) Zhang, X.; Li, J.; Foran, B.; Lee, S.; Guo, H.-Y.; Hogan, T.; Kannewurf, C. R.; Kanatzidis, M. G. *J. Am. Chem. Soc.* **1995**, *117*, 10513−10520.
(9) Patshke, R.; Heising, J.; Brazis, P.; Kannewurf, C. R.; Kanatzidis, M. G. *Chem. Mater.* **1998**, *10*, 695−697.

10.1021/ic991457g CCC: $19.00
Published on Web 03/15/2000

which show the presence of perfect square nets. A close crystallographic examination using electron diffraction invariably reveals subtle modulations which give rise to supercells often incommensurate with the underlying average substructure. For example, electron diffraction measurements on $K_{0.33}Ba_{0.67}AgTe_2$[8] reveal the presence of an incommensurate orthorhombic superstructure of the tetragonal cell with $a_{super} = 2.84a_{sub}$, $b_{super} = b_{sub}$. These modulations are due to distortions in the Te-net which are driven by electronic instabilities which develop in the perfect square nets. Similar superstructures were observed in binary rare earth tellurides and selenides.[10] The type and degree of modulation can vary from compound to compound depending strongly on the number of electrons per Te atom. Besides the electron diffraction experiments, no direct elucidation and refinement of such a structure has been reported so far. Therefore the fine details of the superstructures remain unresolved.

In a previous report,[8] we suggested, on the basis of limited electron diffraction experimentally, crystallographic simulations, and extended-Hückel calculations that the ideal Te-net exhibits a static charge density wave made of V-shaped Te_3^{2-} trimers. Given that no direct crystallographic determination and refinement of an aperiodic structure has been reported before on a square Te-net, we deemed it significant to attempt one in the case of $K_{0.33}Ba_{0.67}AgTe_2$, especially when weak satellite peaks could be occasionally observed in X-ray photographs. Accurate knowledge of the precise aperiodic structure in such compounds will permit a better understanding of the electronic structure and their observed properties. Here, we report the first crystallographic determination of an incommensurate structure of a square Te-net, namely that of $K_{0.33}Ba_{0.67}AgTe_2$, and first principles electronic band structure calculations using the tight-binding linear-muffin-tin-orbital (TB-LMTO) method.[20] The present work identified not only the presence of the V-shaped Te_3 trimer anions, predicted by our earlier work, but also reveals additional significant structural features which could not have been detected by the techniques used earlier. These features include the existence of the rare W-shaped Te_5 pentamer anions. In agreement with the fact that the V-pattern domains are slightly larger than the W-pattern domains in the modulated structure, the band structure calculations indicate that both the V- and W-pattern distortions are stabilizing in nature and that the V-pattern distortion is more stabilizing. In addition, they reveal that, although the nesting vectors of the Fermi surface of the undistorted square-net Te layers are consistent with the observed V- and W-patterns, the stabilization energy is dominated by low lying band levels.

2. Crystal Structure Determination

2.1. Superspace Description of Aperiodic Crystals. The superspace formalism has been introduced for the description of aperiodic crystals, that is, modulated crystal structures, composite crystal structures, and quasicrystals.[11] A modulated crystal structure (the only case considered in this brief introduction to the $(3 + n)$ dimension crystallography) differs from a regular structure by the presence of additional reflections, called satellites, in the diffraction patterns. Those additional spots indicate that a hypothetical "basic structure" having a 3D space group symmetry has been periodically deformed, leading to an incommensurately modulated structure if the periodicity of the modulation is not in a rational ratio with the periodicities of the basic structure. The modulation can originate from a displacement of the atoms (displacive modulation) and/or a deformation of the atomic probability functions (occupation modulation). Although presenting no 3D translational symmetry, an incommensurate structure is not disordered, as shown in ideal cases by the presence of sharp, well separated spots.

Noting that the Fourier wave vectors (Bragg peaks: main reflections and satellites) could be expressed as an integral linear combination of not 3, but $3 + n$ independent vectors, a $(3 + n)$ dimension crystallography was introduced.[12] In this $(3 + n)$ dimension crystallography, an atom position is described by an average position plus a set of periodic atomic modulation functions, often introduced as Fourier series. The atomic occupations and Debye−Waller factors can also be modulated. All the concepts used in 3D crystallography (lattice and metric, point group, space group, etc.) have been extended for the $(3 + n)$ dimension crystallography. In a 3D case, a structure is fully described by giving the lattice and the atomic motif. In a similar way, in an incommensurate $(3 + n)$D case, a structure is fully described by giving the metric (lattice parameters and **q** wavevectors) and the atom descriptions (type, position, occupancy, and Debye−Waller factors and modulation functions for each parameter). A 3D crystal structure, without symmetry translation, can be recovered by looking at a given hyperplane (3D "section") of the $(3 + n)$ dimension periodic space. However, it is worth noticing that the whole structural information is contained within a unit cell of the superspace. For a complete description of the concepts and the notations used for incommensurate structures, see for instance Janssen et al.[11] or van Smaalen[13] and references therein.

2.2. Experimental. 2.2.1. Data Collection. The synthesis of $K_{1/3}Ba_{2/3}AgTe_2$ has already been described elsewhere.[8] From a homogeneous batch, several crystals were tested for quality (intensity and sharpness of the diffraction peaks) with a Weissenberg camera. Numerous crystals revealed very elongated diffraction spots because of crystal curvature. A good, rather large crystal was finally selected and subsequently used for data collection, although no satellites could be detected on the Weissenberg diffraction patterns using regular exposure times. A first data collection was carried out on a STOE image plate system (IPDS) with rather long exposure times (5 min) and a medium resolution (detector distance of 80 mm and phi increment of 1.2°). The averaged cell determined from the stronger Bragg peaks approximately matched that already published (tetragonal cell with $a \approx 4.62$ Å and $c \approx 23.5$ Å),[8] but additional satellites could be clearly observed. Those first order satellites, slightly elongated in shape along c^*, were found in planes parallel to $(h0l)$ and at positions implying both an incommensurate wave vector and a symmetry reduction of the system to at least monoclinic. The cell was then transformed to a more convenient one (giving a **q** vector close to $1/3\mathbf{a}^*$) and a subsequent least-squares refinement from 327 reflection positions by means of U-fit program[14] yielded the lattice parameters $a = 4.6441(10)$ Å, $b = 4.6292(12)$ Å, $c = 23.765(9)$ Å, and $\beta = 101.28(2)°$ with $\mathbf{q} = 0.3248(6)\mathbf{a}^* - 0.071(8)\mathbf{c}^*$. A second data collection was performed on a Nonius CAD-4F diffractometer to collect main reflections at higher $\sin(\theta)/\lambda$

(10) Lee, S.; Foran, B. J. *J. Am. Chem. Soc.* **1996**, *118*, 9139−9147. (b) Foran, B.; Lee, S.; Aronson, M. C. *Chem. Mater.* **1993**, *5*, 974−978. (c) van der Lee, A.; Hoistad, L. M.; Evain, M.; Foran, B.; Lee, S. *Chem. Mater.* **1997**, *5*, 218−226.

(11) Janssen, T.; Janner, A.; Looijenga-Vos, A.; de Wolff, P. M. In *International Tables for X-ray Crystallography, Vol. C: Mathematical, Physical and Chemical Tables*; Wilson, A. J. C., Ed.; Dordrecht: Kluwer Academic Publishers, 1993; Chapter 9.8.

(12) De Wolff, P. M. *Acta Crystallogr.* **1974**, *A30*, 777−785.

(13) van Smaalen, S. *Crystallogr. Rev.* **1995**, *4*, 79−202.

(14) Evain, M. *U-fit*: *a cell parameter refinement program*; Institut des matériaux: Nantes, France, 1992.

Table 1. Crystallographic Data for $K_{0.33}Ba_{0.66}AgTe_2$

(1) Physical, Crystallographic, and Analytical Data		
formula	$K_{0.33}Ba_{0.66}AgTe_2$	
crystal color	light-brown	
molecular weight (g mol^{-1})	467.65	
crystal system	monoclinic	
space group	$P2_1(\alpha 0\gamma)$	
temperature (K)	293	
cell parameters (from 327 reflections collected on IPDS)		
a (Å)	4.6441(10)	
b (Å)	4.6292(12)	β (deg) = 101.28(2)
c (Å)	23.765(9)	
q = 0.248(6)**a*** − 0.071(8)**c***		
V (Å)	501.0(5)	
Z	4	
density (calcd, g cm^{-1})	6.282	
crystal description	plate	
crystal size (mm)	∼0.11× 0.09 × 0.04	

(2) Data Collection		
	Enraf-Nonius CAD-4F	Stoe IPDS
monochromator	oriented graphite (002)	
radiation	MoK-$L_{2,3}$ (λ = 0.7107 Å)	
scan mode	$\omega/2\theta$	ω
no. of measured reflections	10620	6901
hkl range	$-8 \le h \le 8$	$-5 \le h \le 5$
	$-8 \le k \le 8$	$-4 \le k \le 4$
	$-42 \le l \le 42$	$-26 \le l \le 26$
		$-1 \le m \le 1$
sin(θ)/λ range (Å^{-1})	0.44−0.94	0−0.58
no. of standard reflections	3	na
frequency of standard reflections	3600	na

(3) Data Reduction		
	Nonius CAD-4F	Stoe IPDS
linear absorption coeff. (cm^{-1})	209.3	
absorption correction	analytical	
T_{min}/T_{max}	0.18/0.4	0.18/0.4
scaling selection criterion	$I > 10\sigma(I)$	
scaling coefficient (I_{CAD4}/I_{IPDS})	0.1922 (4)	
no. of reflections	8915	
no. of independent reflections	6427 (448 main + 2479 satellite)	
criterions for observed reflections	$I > 3\sigma(I)$	
R_{int} (obs)	0.033	
max sin(θ)/λ	0.8	
no. of observed reflections	2583 (1925 main + 658 satellite)	

(4) Refinement	
refinement	F
F(000)	777
no. of reflections used in the refinement	2583
R^a	0.0330
$R_w{}^a$	0.0367
S	1.47
no. of refined parameters	115
weighting scheme	$w = 1/(\sigma^2\|F_o\|+(0.02\|F_o\|)^2)$
difference Fourier residues	[−2.2, +2.2] e$^-$/ Å

[a] $R = \Sigma||F_o|-|F_c||/\Sigma|F_o|$. $R_w = [\Sigma w(|F_o|-|F_c|)^2/\Sigma w|F_o|^2]^{1/2}$.

values (up to 0.8 Å^{-1}). Intensity loss controls by means of three standard reflections indicated no significant decay and/or fluctuation (lower than 1%). For data collection details, see Table 1.

2.2.2. Data Processing. Data reduction, absorption correction, and refinements were carried out with the JANA98 program package.[15] After the standard Lorentz and polarization effect corrections, the collected intensities were analytically corrected for absorption. Notice that, prior to the absorption correction, the crystal shape and size were optimized on the basis of equivalent reflections with the X-shape program.[16] Both sets (IPDS and CAD4) were then put on a common scale, the scaling factor being established from mutual reflections with $I \ge 10\sigma(I)$. Since the superspace group was later unambiguously determined as $P2_1(\alpha 0\gamma)$, symmetry equivalent reflections of that reflection set were averaged according to the (3 + 1)D point group $(2,\bar{1})$. A set of 6427 reflections (3448 mains and 2479 satellites) with sin(θ)/λ < 0.8 Å^{-1} were then available for structure refinements, out of which 2583 (1925 mains and 658 satellites) were considered as observed under the $I/\sigma(I) > 3.0$ criterion. Systematic absences suggested $P2_1/m(\alpha 0\gamma)$ and $P2_1(\alpha 0\gamma)$ as potential superspace groups. Structure refinements clearly indicated $P2_1(\alpha 0\gamma)$ as the only possible superspace group.

2.2.3. Structure Refinement. Starting from the atomic positions in the assumed tetragonal symmetry obtained by Zhang et al. (1995), the refinement converged to the residual factor R = 0.097 with isotropic displacement parameters (IDP) and symmetry restrictions for Ag, Te1, and K/Ba atoms. Such restrictions were necessary before the ultimate stage of the structure refinement since all the atoms not belonging to the Te sheets almost satisfy a centrosymmetry relation. Introduction of anisotropic displacement parameters (ADP) largely improved the fit with a new residual factor of 0.056. At this stage of the refinement, very large U^{22} ADP terms were noticed for the atoms of the Te sheets (for instance $U^{22} \approx 10 \times U^{33}$ for Te3). With the main reflections only, this refinement could be improved with a splitting of Te3 into two distinct positions, yielding the residual factors R = 0.031 and R_w = 0.048 for 52 parameters. However, to introduce the modulation, the solution with only one Te3 position was preferred as a starting point.

The introduction in the refinement of the satellites and of a combination of a first order displacive modulation and an IDP term for Te3 led to an initial rise of the residual R value for main reflections (0.046) but partially explained the satellite intensities (R = 0.34). An identical development for Te2 resulted in similar, although smaller, improvements (R_{main} = 0.030 and R_{sat} = 0.22). It is worth noticing that, to prevent important correlations obviously linked to the pseudosymmetric character of the structure, refinements were thereafter carried out with all reflections (observed and nonobserved). A release of the coordinate restrictions on Te1, Ag, and K/Ba atoms (initially introduced because of the pseudocentrosymmetry of the structure) and the introduction of displacive first order modulations for those atoms did not greatly reduce the residual factors. In fact, Fourier difference map analyses indicated residues around Te3 and therefore the necessity of increasing the number of displacive modulation waves for Te3 only. Successive introduction of modulation waves enhanced the structure refinement (R = 0.034 for all reflections, 0.025 for mains and 0.105 for satellites, with waves up to the fourth order and 116 parameters). However, in the absence of high order satellites, one cannot add a large number of extra parameters through successive additions of modulation waves without checking the coherence of the results. In the present case, i.e., with the use of up to the fourth order Fourier series displacive modulation waves, a negative Te3 IDP and widespread Te−Te distances within the Te sheets were found, which cannot lead to an easy interpretation in terms of Te contact patterns. A new model had to be looked for.

(15) Petricek, V.; Dusek, M. *JANA98*; Institute of Physics, Academy of Sciences of the Czech Republic: Czech Republic, 1998.

(16) Stoe *X-Shape: crystal optimization for numerical absorption*; STOE & Cie GmbH: Darmstadt, Germany, 1996.

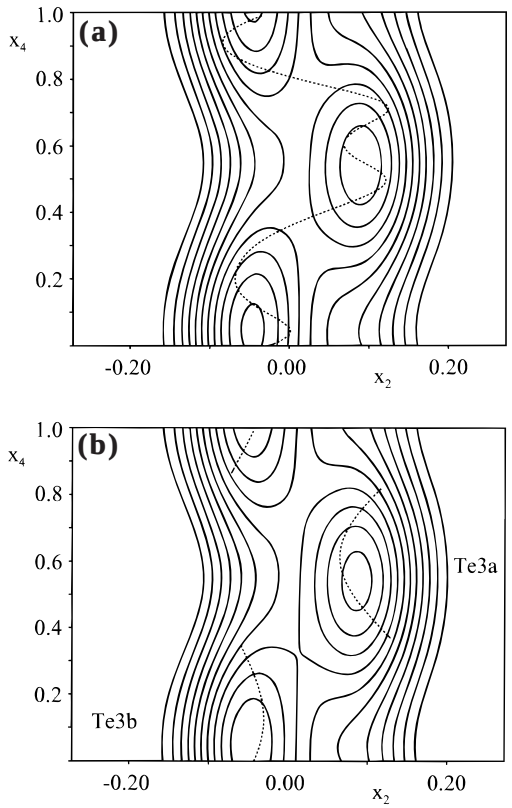

Figure 1. x_2x_4 section at $x_1 = 0$ and $x_3 = 1/4$ of the contour F_{obs} maps around Te3. (a) Model with Fourier series displacive waves only for Te3 (dashed line). (b) Model with a crenel function splitting Te3 into Te3a and Te3b (dashed line). Contour lines in intervals of 15 $e^-/Å^{-3}$.

An analysis of the (x_2,x_4) Fourier map plane around Te3 revealed a split of that Te3 atom into two well-defined positions (see Figure 1a). A convenient way to model this split was to use a built-in crenel function.[17,18] Indeed, a crenel function provides a good way to model a discontinuity in a (3 + 1)D atomic position and avoids intermediate states at the discontinuity, necessarily introduced by a Fourier series description of the modulation. In addition, it leads to a more coherent set of distances with fewer parameters. A splitting of Te3 into Te3a and Te3b was therefore initiated with proper conditions, i.e., a complementarity of the two Te3 crenels. To prevent severe correlations linked to the application of crenel functions to modulation functions, inherently not defined for all values and thus with an orthogonality condition not fulfilled for the set of harmonic functions, an orthogonalization procedure was applied.[17] With such a model the refinement smoothly converged to the following final residual factors: $R = 0.033$ and $R_w = 0.037$ ($R = 0.023$ and $R_w = 0.032$ for mains and $R = 0.101$ and $R_w = 0.100$ for first order satellites) for 2583 observed reflections and 115 parameters. Although very similar to the first structural model with Fourier series waves only (see Figure 1 the F_{obs} map around Te3), this new model does not lead to nondefinite ADP and generates a more homogeneous set of distances with easily interpretable Te contact patterns within the Te sheets (see below).

Attempts to introduce second-order displacive waves for either the Te atoms of the Te layers or the Ag, Te, or K/Ba atoms of the remaining part of the structure did not improve the refinement. Similarly, finding a correlation of the K and Ba site occupation with the Te displacement in the neighboring sheet by means of occupation waves was not possible. Therefore, the last model with first-order displacive waves for all atoms, ADPs for all atoms but Te3a and Te3b, and ADP constraints for atoms related by the pseudo inversion center and the Te3a/Te3b couple was considered as the best model possible for the current data set. Notice that the model does not generate significant second-order satellite intensities, as checked with the overlap option of the refinement program. Final parameters for this incommensurate model are gathered in Tables 2−6.

Table 2. Final Residual Factors for $K_{0.33}Ba_{0.66}AgTe_2$

	N	*R*	R_w
main	1925	0.0236	0.0323
first order	658	0.1008	0.1001
overall	2583	0.0330	0.0367

Table 3. Fractional Atomic Coordinates and Equivalent Isotropic Displacement Parameters[a] (Å^2) for $K_{0.33}Ba_{0.66}AgTe_2$

	x	*y*	*z*	B_{eq}	τ
Te2	0.04974(4)	0.04974(6)	0.25004(9)	1.18(2)	
Te3a	−0.0025(7)	0.0867(6)	0.2503(2)	0.88(2)[b]	
Te3b	−0.0001(7)	−0.0446(6)	0.2506(2)	0.88[b]	
Ag1a	0.7506(4)	−0.0050(7)	−0.00022(9)	2.19(1)	
Ag1b	0.2509(4)	0.0037(7)	0.50002(9)	2.19	
Te1a	0.8264(3)	0.4981(6)	0.07542(6)	1.32(1)	
Te1b	0.1754(3)	0.4998(6)	0.42445(6)	1.32	
Ba1	0.3772(3)	−0.0017	0.13219(7)	1.29(3)	0.645(7)
Ba2	0.6138(3)	−0.0013(9)	0.36834(7)	1.31(3)	0.666(8)
K1	0.3772	−0.0017	0.13219	1.29	0.355
K2	0.6138	−0.0013	0.36834	1.31	0.334

[a] $B_{eq} = 8\pi^2/3\sum_i\sum_j U^{ij} a_i^* \times a_j^* \times \mathbf{a}_i \times \mathbf{a}_j$. [b] B_{iso}.

2.3. Crystal Structure Analysis. The $K_{1/3}Ba_{2/3}AgTe_2$ structure has been described in detail in the original publication reporting the average structure.[8] Let us briefly indicate its main characteristics. The structure is built up from the alternation of two different covalent layers, a $[Ag_2Te_2]^{2-}$ layer and a $[Te_2]^{4/3-}$ layer, both layers being separated by a K/Ba cation plane (see the average structure presented in Figure 2). The $[Ag_2Te_2]^{2-}$ is of the anti-PbO type, which is the basic construction of any $ThCr_2Si_2$ type structure, whereas the $[Te_2]$ layer derives from a square net.

Since the $[Ag_2Te_2]$ layer is only weakly modulated, the Ag−Te calculated distances within this layer (see Table 7) are very close to those already reported for the averaged structure (2.90 Å in averaged to be compared with 2.91 Å). In the same way, the Ba/K closest contacts with the Te atoms of the $[Ag_2Te_2]$ layers are almost identical to those already found (ca. 3.52 Å). As earlier stated in the experimental part, the major difference between the average and the modulated structures is found in the $[Te_2]$ layers.

In parts a and b of Figure 3 are presented the Te2−Te3x distance curves for the two studied models (one and two Te3 positions, respectively). Before the splitting of the atom sites Te3 by means of the crenel function, two sets of distances are mainly observed, around 2.9 Å and around 3.6 Å (Figure 3a). However, intermediate distances appear in short *t* intervals centered at $t \approx 0.4$ and $t \approx 0.8$. Those latter distances are directly linked to the crenel-like shape of the Te3 *y* modulation, as noticed in Figure 1b (note that, for Te3, $x_4 \approx t$ since $\mathbf{q}\cdot\mathbf{r} \approx 0$). After the splitting of Te3, the two sets of Te−Te distances are more apparent (Figure 3b), although intermediate distances are still present around $t = 0.1$. With 3.1 Å as a upper contact cutoff, two Te patterns are essentially observed: a "V" and a "W" pattern (see Figure 4). The "V" pattern arrangement corresponds

(17) Boucher, F.; Evain, M.; Petricek, V. *Acta Crystallogr.* **1996**, *B56*, 100−109.
(18) Petricek, V.; van der Lee, A.; Evain, M. *Acta Crystallogr.* **1995**, *A51*, 529−531.

Table 4. Anisotropic Displacement Parameters U^{ij} [a] (Å^2) for $K_{0.33}Ba_{0.66}AgTe_2$

	U^{11}	U^{22}	U^{33}	U^{12}	U^{13}	U^{23}
Te2	0.0101(4)	0.0199(5)	0.01460(12)	0.0000(10)	0.0018(2)	−0.0009(9)
Ag1a	0.0283(2)	0.0323(2)	0.02226(14)	0.0006(7)	0.0039(2)	0.0048(6)
Ag1b	0.0283	0.0323	0.02226	0.0006	0.0039	0.0048
Te1a	0.01258(8)	0.01430(10)	0.02357(11)	0.0008(5)	0.00459(7)	0.0001(5)
Te1b	0.01258	0.01430	0.02357	0.0008	0.00459	0.0001
Ba1/K1	0.0148(5)	0.0176(8)	0.0159(6)	−0.0008(5)	0.00459(7)	0.0001(5)
Ba2/K2	0.0146(5)	0.0157(8)	0.0210(6)	0.0006(7)	0.0068(4)	0.0020(7)

[a] The anisotropic displacement factor exponent takes the form $(-2\pi^2\sum_i\sum_j U^{ij}\times a_i^*\times a_j^*\times h_i\times h_j)$.

Table 5. Atomic Positional and DWF Modulation Coefficients[a] for $K_{0.33}Ba_{0.66}AgTe_2$

Te2		
$U^{Te2}_{x,s1} = 0.0252(5)$	$U^{Te2}_{y,s1} = 0.0222(8)$	$U^{Te2}_{z,s1} = 0.0007(1)$
$U^{Te2}_{x,c1} = -0.0111(9)$	$U^{Te2}_{y,c1} = 0.0335(5)$	$U^{Te2}_{z,c1} = 0.0001(2)$
Te3a		
$U^{Te3a}_{x,0} = 0.0155(6)$	$U^{Te3a}_{y,0} = 0.009(2)$	$U^{Te3a}_{z,0} = 0.0006(2)$
$U^{Te3a}_{x,1} = -0.0091(11)$	$U^{Te3a}_{y,1} = 0.0170(9)$	$U^{Te3a}_{z,1} = 0.0015(2)$
Te3b		
$U^{Te3b}_{x,0} = -0.0336(5)$	$U^{Te3b}_{y,0} = 0.0081(11)$	$U^{Te3b}_{z,0} = -0.0009(2)$
$U^{Te3b}_{x,1} = 0.0036(10)$	$U^{Te3b}_{y,1} = 0.0086(10)$	$U^{Te3b}_{z,1} = -0.0031(2)$
Ag1a		
$U^{Ag1a}_{x,s1} = -0.0117(11)$	$U^{Ag1a}_{y,s1} = 0.0011(5)$	$U^{Ag1a}_{z,s1} = -0.0007(2)$
$U^{Ag1a}_{x,c1} = 0.0010(8)$	$U^{Ag1a}_{y,c1} = 0.007(2)$	$U^{Ag1a}_{z,c1} = 0.0001(2)$
Ag1b		
$U^{Ag1b}_{x,s1} = -0.0145(11)$	$U^{Ag1b}_{y,s1} = 0.0020(5)$	$U^{Ag1b}_{z,s1} = -0.002(2)$
$U^{Ag1b}_{x,c1} = 0.0022(9)$	$U^{Ag1b}_{y,c1} = 0.0044(13)$	$U^{Ag1b}_{z,c1} = 0.0004(1)$
Te1a		
$U^{Te1a}_{x,s1} = 0.0029(7)$	$U^{Te1a}_{y,s1} = 0.0015(5)$	$U^{Te1a}_{z,s1} = -0.0001(2)$
$U^{Te1a}_{x,c1} = -0.0026(7)$	$U^{Te1a}_{y,c1} = 0.0051(5)$	$U^{Te1a}_{z,c1} = -0.0009(2)$
Te1b		
$U^{Te1b}_{x,s1} = -0.0017(7)$	$U^{Te1b}_{y,s1} = 0.0029(5)$	$U^{Te1b}_{z,s1} = 0.0004(2)$
$U^{Te1b}_{x,c1} = -0.0004(7)$	$U^{Te1b}_{y,c1} = 0.0031(5)$	$U^{Te1b}_{z,c1} = 0.0009(2)$
Ba1/K1		
$U^{Ba1/K1}_{x,s1} = -0.0034(10)$	$U^{Ba1/K1}_{y,s1} = 0.0039(6)$	$U^{Ba1/K1}_{z,s1} = -0.0004(2)$
$U^{Ba1/K1}_{x,c1} = -0.0001(9)$	$U^{Ba1/K1}_{y,c1} = 0.0155(6)$	$U^{Ba1/K1}_{z,c1} = -0.0007(2)$
Ba2/K2		
$U^{Ba2/K2}_{x,s1} = -0.0080(10)$	$U^{Ba2/K2}_{y,s1} = 0.0063(6)$	$U^{Ba2/K2}_{z,s1} = 0.0012(2)$
$U^{Ba2/K2}_{x,c1} = 0.0024(8)$	$U^{Ba2/K2}_{y,c1} = 0.0094(6)$	$U^{Ba2/K2}_{z,c1} = 0.0003(2)$

[a] Modulation functions, up to the *k*th order, for a parameter λ of an atom ν defined in a restricted interval (case of Te3a and Te3b) are given by $U^{\nu}_{\lambda}(\bar{x}_4) = \sum_{i=0}^{k} U^{\nu}_{\lambda,n}\times\text{ortho}^{\nu}_i(\bar{x}_4)$ obtained from Schmit orthogonalization procedure where the orthogonalized functions are given by $\text{ortho}^{\nu}_i(\bar{x}_4) = B^{\nu}_0 + \sum_{n=1}^{k} A^{\nu}_n\times\sin(2\pi n\bar{x}_4) + \sum_{n=1}^{k} B_n{}^{\nu}\times\cos(2\pi n\bar{x}_4)$. The modulation functions are classically written as $U^{\nu}_{\lambda}(\bar{x}_4) = U^{\nu}_{\lambda,0} + \sum_{n=1}^{k} U^{\nu}_{\lambda,\text{sn}}\times\sin(2\pi n\bar{x}_4) + \sum_{n=1}^{k} U^{\nu}_{\lambda,\text{cn}}\times\cos(2\pi n\bar{x}_4)$. Only independent coefficients are provided.

to the predictions of Zhang et al.[8] from μ_2-Hückel optimization. It is worth noticing that the domains of V patterns are slightly larger than those of W patterns. The 3.1−3.3 Å intermediate Te−Te contacts are found exclusively between the W motifs and the lone Te3b between those W motifs, making chains of short Te contacts (<3.3 Å) along the *a* axis.

3. Band Structure Calculations

3.1. Computational Details. TB-LMTO electronic band structure calculations were carried out for $K_{1/3}Ba_{2/3}AgTe_2$ in the atomic sphere approximation using the LMTO47 program.[20] Exchange and correlation were treated in a local spin density approximation.[21a] All the relativistic effects but spin−orbit coupling were taken into account using a scalar relativistic approximation.[21b]

Table 6. Orthonormalized Set Functions Used for Modulation

$\text{ortho}^{\nu}_i(\bar{x})_4 = B^{\nu}_0 + \sum_{n=1}^{k} A^{\nu}_n\times\sin(2\pi n\bar{x}_4) + \sum_{n=1}^{k} B^{\nu}_n\times\cos(2\pi n\bar{x}_4)$

$\text{ortho}^{\text{Te3a}}_i$	B^{Te3a}_0	A^{Te3a}_1	B^{Te3a}_1
$\text{ortho}^{\text{Te3a}}_0$	1		
$\text{ortho}^{\text{Te3a}}_1$	0.652	1.711	
$\text{ortho}^{\text{Te3a}}_2$	2.390	1.656	3.131
orthogonalized set functions based on crenel $\bar{x}^{\text{Te3a}}_4 = 0.595(2)/\Delta^{\text{Te3a}} = 0.483(2)$			

$\text{ortho}^{\text{Te3b}}_i$	B^{Te3b}_0	A^{Te3b}_1	B^{Te3b}_1
$\text{ortho}^{\text{Te3b}}_0$	1		
$\text{ortho}^{\text{Te3b}}_1$	−0.579	1.620	
$\text{ortho}^{\text{Te3b}}_2$	−1.635	1.295	2.477
orthogonalized set functions based on crenel $\bar{x}^{\text{Te3b}}_4 = 0.104(2)/\Delta^{\text{Te3b}} = 0.517(2)$			

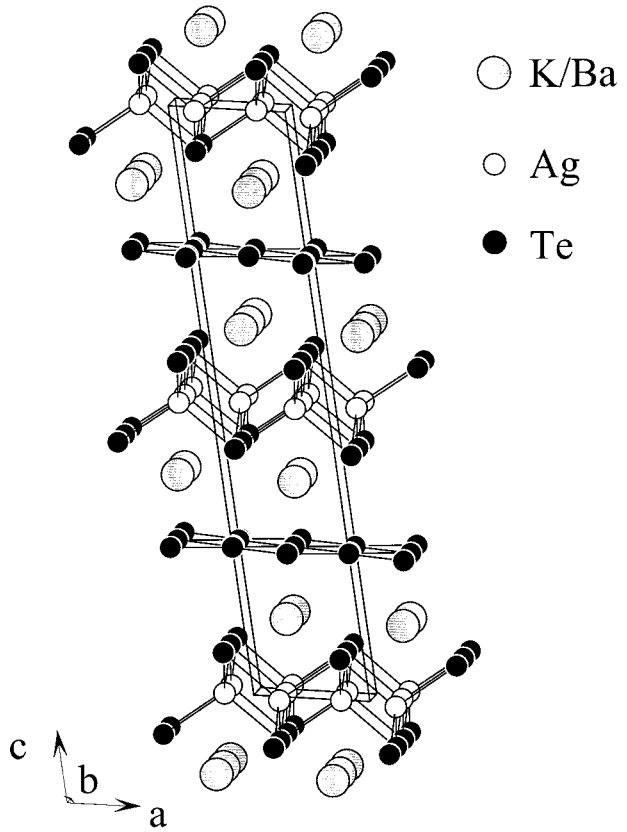

Figure 2. The average structure of $K_{0.33}Ba_{0.66}AgTe_2$.

In the atomic sphere approximation, the space is filled with small overlapping Wigner−Seitz (WS) atomic spheres. The symmetry of the potential is considered spherical inside each WS sphere and a combined correction is used to take into account the overlapping part.[22] The radii of the WS spheres were obtained by requiring that the overlapping potential be

(19) van Smaalen, S. *Crystallogr. Rev.* **1995**, *4*, 79−202.

Table 7. Main Interatomic Distances (Å) for $K_{0.33}Ba_{0.66}AgTe_2$

	average	min	max
Ag1a−Te1a	2.886	2.871	2.901
	2.908	2.885	2.930
	2.902	2.830	2.975
	2.890	2.846	2.934
Ag1b−Te1b	2.881	2.868	2.894
	2.910	2.896	2.925
	2.907	2.849	2.966
	2.893	2.830	2.958
K1/Ba1−Te1a	3.503	3.449	3.556
	3.501	3.466	3.536
	3.539	3.492	3.586
	3.537	3.503	3.571
K2/Ba2−Te1b	3.494	3.457	3.531
	3.500	3.461	3.540
	3.528	3.491	3.565
	3.534	3.505	3.563
K1/Ba1−Te2	3.580	3.529	3.630
	3.576	3.478	3.670
K2/Ba2−Te2	3.590	3.514	3.665
	3.583	3.484	3.679
K1/Ba1−Te3a	3.605	3.527	3.780
	3.619	3.548	3.749
K1/Ba1−Te3b	3.585	3.486	3.797
	3.612	3.498	3.865
K2/Ba2−Te3a	3.609	3.532	3.686
	3.623	3.435	3.711
K2/Ba2−Te3b	3.569	3.324	3.679
	3.588	3.419	3.669

the best possible approximation to the full potential and were determined by an automatic procedure described in ref 22. This overlap should not be too large because the error in the kinetic energy introduced by the combined correction is proportional to the fourth power of the relative sphere overlap. The interatomic space was filled with interstitial spheres since the structures of the compound under examination are not closely packed. The optimal positions and radii (r_{ES}) of these "empty spheres" were determined according to the method described in ref 22. In total, 19 empty spheres with $0.76 \leq r_{ES} \leq 1.32$ Å were introduced for the average structure of $K_{1/3}Ba_{2/3}AgTe_2$. This made the maximum relative overlap between two adjacent atomic spheres less than 16%. Calculations for the distorted

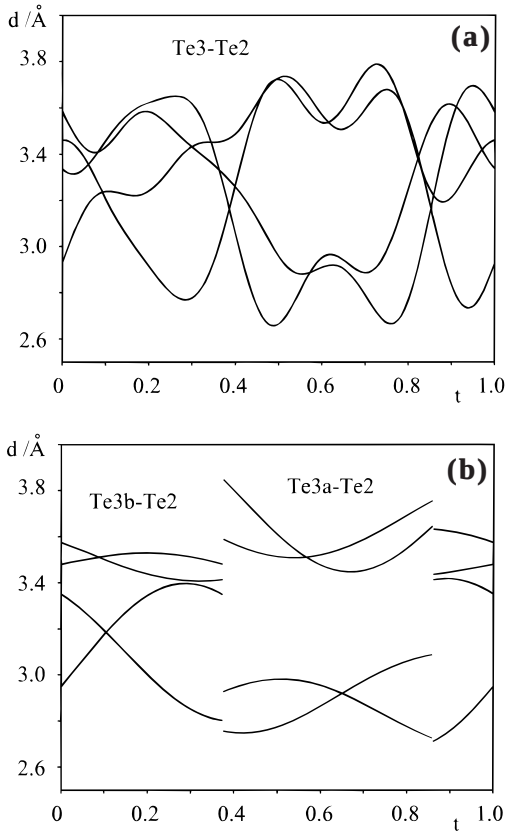

Figure 3. Te3−Te2 distances (Å) as a function of the internal coordinate *t*. (a) Model with Fourier series displacive waves only for Te3. (b) Model with a crenel function splitting Te3 into Te3a and Te3b.

structures (see below) were performed using a slightly higher overlap limit (i.e., less than 17%) by employing 12 empty spheres with $1.30 \leq r_{ES} \leq 1.45$ Å. We used three model structures of $K_{1/3}Ba_{2/3}AgTe_2$: model 1 for the average structure and models 2 and 3 for the distorted structure (see below for the definitions of models 1−3). The positions and radii of the WS spheres used for models 1−3 are specified in notes 23−25, respectively.

The basis set included Te 5s, 5p, 5d, and 4f orbitals, Ag 5s, 5p, 4d, and 4f orbitals, Ba 6s, 6p, 5d, and 4f orbitals, and K 4s, 4p, 3d, and 4f orbitals. Depending of the size of the WS spheres, we used empty sphere s, p, and d orbitals or, for sphere radii smaller than 1.0 Å, only empty sphere s and p orbitals. The Te 5d and 4f orbitals, the Ag 4f orbital, the Ba 6p and 4f orbitals, the K 4p, 3d and 4f orbitals, and the empty sphere d orbitals were treated by the Löwdin downfolding technique.[20] The

(20) Andersen, O. K. *Phys. Rev. B* **1975**, *12*, 3060−3083. (b) Andersen, O. K.; Jepsen, O.*Phys. Rev. Lett.* **1984**, *53*, 2571−2574. (c) Andersen, O. K.; Jepsen, O.; Glötzel, D., In *Highlights of condensed-matter theory*; Bassani, F., Fumi, F., Tosi, M. P., Lambrecht, W. R. L., Eds.; North-Holland: New York, 1985. (d) Andersen, O. K. *Phys. Rev. B* **1986**, *34*, 2439−2449.

(21) von Barth, U.; Hedin, L. *J. Phys. C* **1972**, *5*, 1629−1642. (b) Koelling, D. D.; Harmon, B. N. *J. Phys. C* **1977**, *10*, 3107−3114.

(22) Jepsen, O.; Andersen, O. K. *Z. Phys. B* **1995**, *97*, 35−47.

(23) Data used for the band structure calculations on $K_{1/3}Ba_{2/3}AgTe_2$, model 1 are as follows: space group, *Pm*; cell parameters, $a = 4.6233$ Å, $b = 4.6079$ Å, $c = 23.2026$ Å, $\beta = 90.0°$; atomic sphere radii (Å) and positions, K1 (2.13// 0.2476; 1/2; 0.8682), K2 (2.14// 0.7520; 0; 0.3678), Ba1 (2.13// 0.7524; 0; 0.1318), Ba2 (2.13// 0.2480; 1/2; 0.6322), Ag1 (1.58// 0.2458; 0; 0.9995), Ag2 (1.58// 0.7542; 1/2; 0.0005), Ag3 (1.58// 0.2463; 0; 0.4998), Ag4 (1.58//0.7537; 1/2; 0.5002), Te1 (1.76// 0.7499; 0; 0.9243), Te2 (1.76// 0.2501; 1/2; 0.0757), Te3 (1.84// 0.2765; 0; 0.2498), Te4 (1.82// 0.2498; 0; 0.7471), Te5 (1.84// 0.7235; 1/2; 0.7502), Te6 (1.82// 0.7502; 1/2; 0.2529), Te7 (1.77// 0.7501; 0; 0.5752), Te8 (1.77// 0.2499; 1/2; 0.4248); empty sphere radii (Å) and positions, E (1.32// 0.2502; 1/2; 0.3117), E1 (1.32// 0.7498; 0; 0.6884), E2 (1.34// 0.7598; 0; 0.8106), E3 (1.34// 0.2401; 1/2; 0.1895), E4 (0.86// 0.6823; 0; 0.4794), E5 (0.86// 0.3175; 1/2; 0.5206), E6 (0.86// 0.6817; 0; 0.0201), E7 (0.86// 0.3184; 1/2; 0.9799), E8 (0.84// 0.2221; 1/2; 0.7447), E9 (0.84// 0.7778; 0; 0.2553), E10 (0.72// 0.5916; 1/2; 0.1626), E11 (0.72// 0.4083; 0; 0.8374), E12 (0.75// 0.7185; 1/2; 0.4140), E13 (0.75// 0.2812; 0; 0.5860), E14 (0.75// 0.7170; 1/2; 0.0863), E15 (0.75// 0.2832; 0; 0.9136), E16 (0.74// 0.2520; 0; 0.4134), E17 (0.74// 0.7480; 1/2; 0.5866), E18 (0.76// 0.2524; 0; 0.0859).

(24) Data used for the band structure calculations on $K_{1/3}Ba_{2/3}AgTe_2$, model 2 are as follows: space group, $P2_1$; cell parameters, $a = 13.8699$ Å, $b = 4.6079$ Å, $c = 23.6596$ Å, $\beta = 101.28°$; atomic sphere radii (Å) and positions, Te1 (1.77// 0.0582; 0.2474; 0.4245), Te2 (1.77// 0.3915; 0.2474; 0.4245), Te3 (1.77// 0.7248; 0.2474; 0.4245), Te4 (1.74// 0.9418; 0.2465; 0.0755), Te5 (1.74// 0.6085; 0.2465; 0.0755), Te6 (1.74// 0.2751; 0.2465; 0.0755), Te7 (1.67// 0.8312; 0.7926; 0.7495), Te8 (1.74// 0.5053; 0.2289; 0.2502), Te9 (1.68// 0.8238; 0.2340; 0.2494), Te10 (1.73// 0.9890; 0.2076; 0.7501), Te11 (1.67// 0.6789; 0.2106; 0.7479), Te12 (1.68// 0.6670; 0.8235; 0.2485), Ag1 (1.56// 0.5799; 0.2337; 0.4997), Ag2 (1.56// 0.9132; 0.2337; 0.4997), Ag3 (1.56// 0.2465; 0.2337; 0.4997), Ag4 (1.54// 0.5869; 0.7702; 0.0001), Ag5 (1.54// 0.9203; 0.7702; 0.0001), Ag6 (1.54// 0.2536; 0.7702; 0.0001), Ba1 (2.32// 0.5393; 0.7540; 0.3683), Ba2 (2.32// 0.8726; 0.7540; 0.3683), Ba3 (2.36// 0.5395; 0.2427; 0.8677), Ba4 (2.34// 0.8728; 0.2427; 0.8677), K1 (2.32// 0.2059; 0.7540; 0.3683), K2 (2.36// 0.2061; 0.2427; 0.8677); empty sphere radii (Å) and positions, E (1.45// 0.3143; 0.2069; 0.1931), E1 (1.42// 0.3547; 0.2105; 0.3072), E2 (1.41// 0.0073; 0.2076; 0.3077), E3 (1.41// 0.9684; 0.2048; 0.1912), E4 (1.39// 0.3541; 0.8360; 0.8104), E5 (1.34// 0.3049; 0.8621; 0.6879).

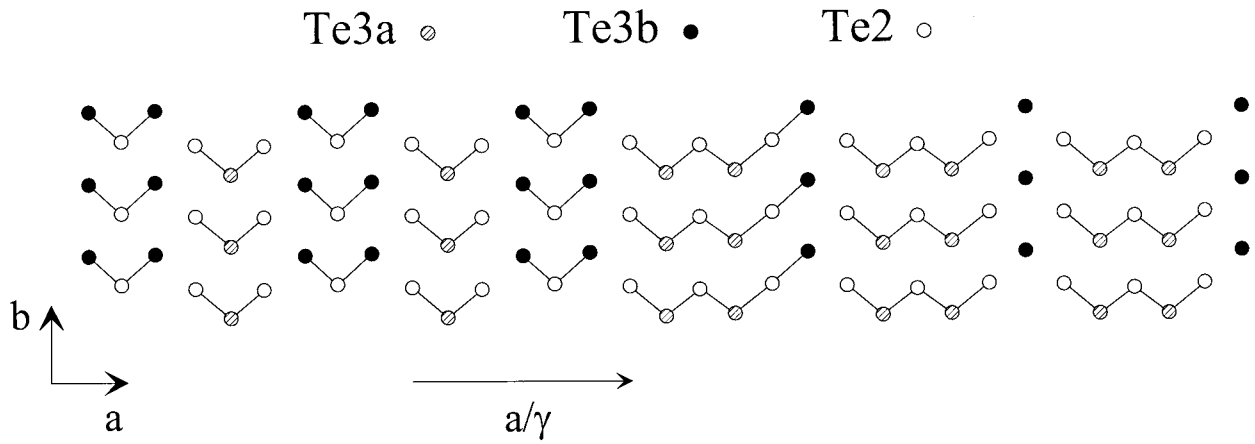

Figure 4. Fragment of a Te sheet showing the Te−Te short contacts calculated at a 3.1 Å cutoff. Two motifs are observed: Te groups with a "V" shape and Te groups with a "W" shape. Occasionally, as the motif changes from V to W, the lone Te3b atom found between two W motifs is at a distance slightly shorter than 3.1 Å of a W motif (one such example is observed in the figure).

k-space integrations were performed by the tetrahedron method.[26] The self-consistent charge density was obtained using 80 irreducible k-points for the average structure, and 24 irreducible k-points for the distorted structure. The contribution of the nonspherical part of the charge density to the potential was neglected.

3.2. Electronic Structure Analysis. The incommensurately modulated crystal structure of $K_{1/3}Ba_{2/3}AgTe_2$ cannot be described by electronic band structure calculations. Thus we carried out electronic band structure calculations for three commensurate structures of $K_{1/3}Ba_{2/3}AgTe_2$, i.e., one average structure and two commensurately distorted structures.

3.2.1. Average Structure. The averaged structure, i.e., the monoclinic 3D structure ($P2_1/m$ space group) shown in Figure 2 can be regarded as the undistorted structure with a tetragonal-like unit cell (in this representation the modulation vector is $\mathbf{q} = 0.3248\mathbf{a}^* + 0.2538\mathbf{c}^*$). For electronic band structure calculations, an ordered distribution of the K and Ba atoms is needed. For this purpose, we consider an ordered structure with the composition $K_{1/2}Ba_{1/2}AgTe_2$ (using the space group *Pm*, a subgroup of $P2_1/m$) in which each AgTe- and each Te-layer is surrounded by one potassium layer and one barium layer. To make this compound isoelectronic to $K_{1/3}Ba_{2/3}AgTe_2$, we consider the charged structure $[K_{1/2}Ba_{1/2}AgTe_2]^{(1/6)+}$. The electronic structure of the latter charged compound was determined self-consistently. This approximation assumes implicitly that the cations K^+ and Ba^{2+} have no strong influence on the electronic structure of $K_{1/3}Ba_{2/3}AgTe_2$, and their primary role is ionic. Hereafter, the commensurate average structure defined above will be referred to as model 1.

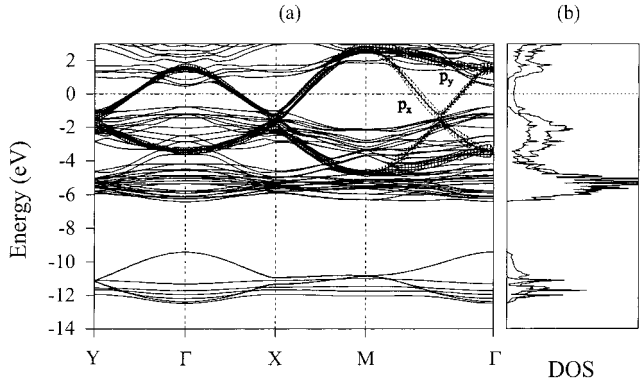

Figure 5. Electronic band structure calculated for the average structure (model 1) of $K_{1/3}Ba_{2/3}AgTe_2$. (a) Dispersion relations, where $\Gamma = (0,0,0)$, $X = (a^*/2,0,0)$, $Y = (0,b^*/2,0)$, and $M = (a^*/2,b^*/2,0)$. The p_x and p_y orbital contributions of the Te layer are visualized with a "fat band" representation. (b) Total DOS plot and projected DOS plot calculated for the AgTe layer.

The electronic band structure calculated for model 1 is presented in Figure 5. The band dispersion is very weak along the $\mathbf{c}^*$ direction, so only the high-symmetry in-plane directions are considered in Figure 5a. The total density of states (DOS) and the projected DOS corresponding to the AgTe-layers are also shown in Figure 5b. Notice that the Fermi level is used as the origin of the energy axis. In the energy region between −13 and −9 eV, the crystal orbitals are essentially Te s orbitals in character and the two most dispersive bands have the Te s orbital character of the Te-layer. Between −6.5 and −4 eV are found the Ag d orbitals. The Te p orbitals of the AgTe layers cover the energy range between −4 and −1 eV. The p orbitals of the Te-layers occur in a wide energy region, between −5 and 3 eV. All the Te p_z orbitals are occupied, but this is not the case for the Te p_x and p_y orbitals. This is in agreement with the charge balance $(K^+)_{1/3}(Ba^{2+})_{2/3}(Ag^+Te^{2-})(Te)^{(2/3)-}$ proposed by Zhang et al.[8] The first strongly antibonding bands above the Fermi level are chiefly Ag s orbitals in character.

In Figure 5a, the bands of the Te p_x and p_y orbitals, indicated by a "fat band" representation, cross the Fermi level. (In a fat band representation, the thickness of a dispersion curve at a given k-point is made proportional to the contribution of an orbital character under examination.) Here, to classify the symmetry of the Te p orbitals, we used the local Cartesian axes

(25) Data used for the band structure calculations on $K_{1/3}Ba_{2/3}AgTe_2$, model 3 are as follows: space group, $P2_1$; cell parameters, $a = 13.8699$ Å, $b = 4.6079$ Å, $c = 23.6596$ Å, $\beta = 101.28°$; atomic sphere radii (Å) and positions, Te1 (1.78// 0.0582; 0.2474; 0.4245), Te2 (1.78// 0.3915; 0.2474; 0.4245), Te3 (1.78// 0.7248; 0.2474; 0.4245), Te4 (1.75// 0.9418; 0.2465; 0.0755), Te5 (1.75// 0.6085; 0.2465; 0.0755), Te6 (1.75// 0.2751; 0.2465; 0.0755), Te7 (1.83// 0.8406; 0.7754; 0.7501), Te8 (1.84// 0.4924; 0.7720; 0.7494), Te9 (1.61// 0.8311; 0.2121; 0.2496), Te10 1.67// 0.9917; 0.8463; 0.2507), Te11 (1.89// 0.6697; 0.2267; 0.7530), Te12 (1.61// 0.6719; 0.8622; 0.2518), Ag1 (1.57// 0.5799; 0.2337; 0.4997), Ag2 (1.57// 0.9132; 0.2337; 0.4997), Ag3 (1.57// 0.2465; 0.2337; 0.4997), Ag4 (1.55// 0.5869; 0.7702; 0.0001), Ag5 (1.55// 0.9203; 0.7702; 0.0001), Ag6 (1.55// 0.2536; 0.7702; 0.0001), Ba1 (2.30// 0.5393; 0.7540; 0.3683), Ba2 (2.33// 0.8726; 0.7540; 0.3683), Ba3 (2.27// 0.5395; 0.2427; 0.8677), Ba4 (2.23// 0.8728; 0.2427; 0.8677), K1 (2.32// 0.2059; 0.7540; 0.3683), K2 (2.37// 0.2061; 0.2427; 0.8677); empty sphere radii (Å) and positions, E (1.43// 0.9938; 0.8377; 0.6919), E1 (1.40// 0.3439; 0.8230; 0.8104), E2 (1.42// 0.3010; 0.8379; 0.6906), E3 (1.41// 0.0302; 0.8214; 0.8102), E4 (1.34// 0.3436; 0.2266; 0.3108), E5 (1.30// 0.3277; 0.2266; 0.1866).

(26) Blöchl, P. E.; Jepsen, O.; Andersen, O. K. *Phys. Rev. B* **1994**, *49*, 16223−16233.

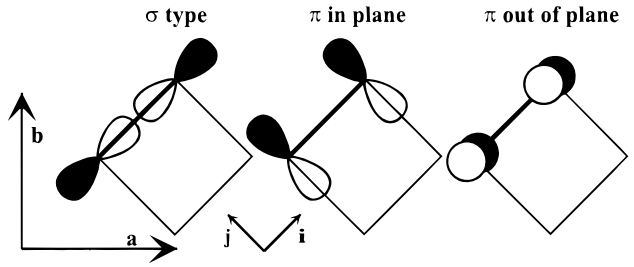

Figure 6. Local Cartesian axes used to define the Te p_x, p_y, and p_z orbitals of the Te layer.

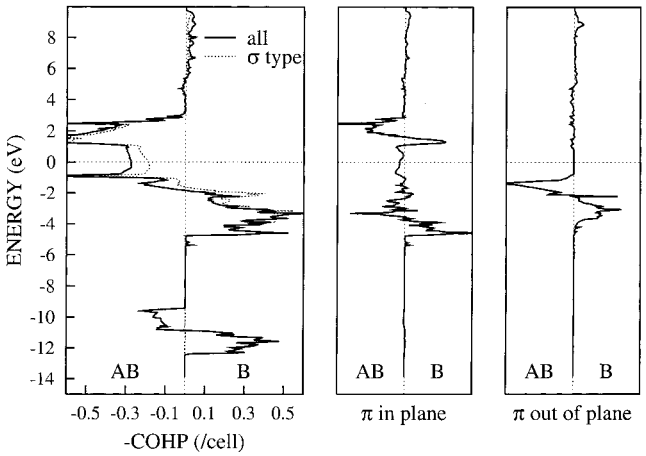

Figure 7. Crystal orbital Hamiltonian population (COHP) of the Te−Te interactions calculated for the Te layers in the average structure (model 1) of $K_{1/3}Ba_{2/3}AgTe_2$. Orbital decompositions were carried out according to the local Cartesian system defined in Figure 3.

shown in Figure 6. The strong interaction between the in-plane Te p orbitals are responsible for the strong dispersion. The bands of the Te p_x and p_y orbitals meet each other at the *X* and *Y* symmetry points and around the midpoint of the M-Γ line. A crystal orbital Hamiltonian population analysis[27] carried out for the interactions between two neighboring tellurium atoms of the Te-layer ($d_{Te-Te} = 3.18$ Å) is summarized in Figure 7 based on the orbital classification of Figure 6. An antibonding character starts to occur above −1.6 eV for the σ type interactions, above −2.2 eV for the out-of-plane π interaction, and above −3.5 eV for the in-plane π interaction. Thus, in the average structure, the occupied energy levels in the vicinity of the Fermi level are antibonding in nature.

Figure 8 shows the Fermi surface calculated for model 1. The Fermi surface is comparable in shape to the surface presented by Zhang et al.[8] and obtained by means of the simple Hückel method through a 2D calculation. For comparison, the ideal Fermi surface calculated by Lee and Foran[10a] considering only the σ type interactions between the first neighbor Te atoms is also shown by dashed line on the upper right part of Figure 8. The ideal Fermi surface is nested by the vector $\mathbf{k}_3 = \mathbf{a}^*/3$ or $\mathbf{b}^*/3$, which is quite close to the in-plane component of the modulation vector **q** of the incommensurately distorted structure of $K_{1/3}Ba_{2/3}AgTe_2$ ($\mathbf{q} = 0.3248\mathbf{a}^* + 0.2538\mathbf{c}^*$). The Fermi surface obtained from extended Hückel calculations does not consist of straight lines but of sinusoidal wavy lines.[8] Zhang et al. suggested that the vector $\mathbf{k}_3$ is still relevant for this "warped" Fermi surface. The Fermi surface of the present study deviates more strongly from the ideal Fermi surface and hence makes it unreasonable to regard $\mathbf{k}_3$ as a true nesting vector (see Figure 9a). Instead, the vectors $\mathbf{k}_1 \propto 1/6(\mathbf{a}^* + \mathbf{b}^*)$ and $\mathbf{k}_2 \propto 1/6(\mathbf{a}^* - \mathbf{b}^*)$ provide a perfect nesting (see parts b and c of Figure 9). The Te-layers of $K_{1/3}Ba_{2/3}AgTe_2$ can be regarded as consisting of parallel Te chains along the ($\mathbf{a}^* + \mathbf{b}^*$) and ($\mathbf{a}^* - \mathbf{b}^*$) directions. The vectors $\mathbf{k}_1$ and $\mathbf{k}_2$ imply a 3-fold superstructure along these diagonal directions. This is consistent with the occurrence of both the V- and W-pattern distortions as depicted in Figure 10 and a direct interpretation of the bonding pattern can be obtained with these nesting vectors.

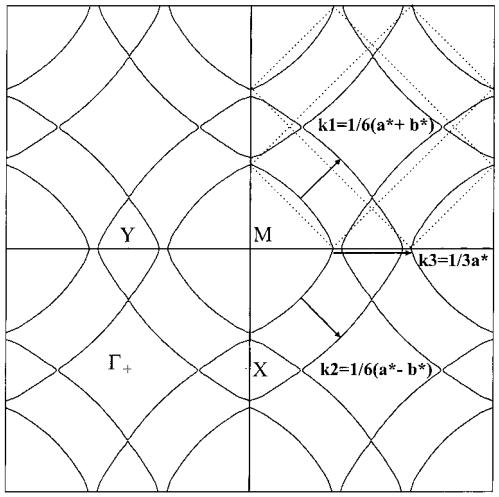

Figure 8. Fermi surface calculated for the average structure (model 1) of $K_{1/3}Ba_{2/3}AgTe_2$. The dashed lines on the upper right part show the ideal Fermi surface obtained from simple Hückel calculations considering only the σ type interactions between the first neighbor Te atoms.

To understand the sinusoidal warping of the Fermi surface (from the viewpoint of the ideal Fermi surface), it is necessary to consider the in-plane π type interactions between the parallel chains (see Figures 5a and 6). Figure 11 shows how the intrachain (σ type) and the interchain (π type) interactions affect the band dispersion along the Γ-M line for the four bands of the Te p_x and p_y orbitals. For bonding intrachain interactions, the interchain interactions are bonding at M and antibonding at Γ. In contrast, for antibonding intrachain interaction, the interchain interactions are antibonding at M and bonding at Γ. Thus, the two bands of the p_x orbitals cross at a k-point closer to Γ than M along the Γ-M line, i.e., not at the midpoint of the Γ-M line. This asymmetry of the band dispersion is responsible for the sinusoidal warping of the Fermi surface.

3.2.2. Distorted Structure. We simulate the incommensurate structure of $K_{1/3}Ba_{2/3}AgTe_2$ with two commensurate structures. Model 2 has only the V-pattern distortion in the Te-layers, and model 3 only the W-pattern distortion. Both models have a $P2_1$ symmetry and a tripled unit cell with respect to the unit cell of model 1. Since the contributions of the K/Ba orbitals upon the electronic structure to the AgTe and Te-layers are negligible, we replace the statistical distribution of K/Ba in each model with an ordered K/Ba arrangement. Both models gave similar results, as described below.

Figure 12a shows the electronic band structure calculated for the distorted structure of model 2 (V-pattern distortion), and Figure 13a that for the distorted structure of model 3 (W-pattern distortion). The electronic structures of models 2 and 3 have an indirect band gap (0.43 and 0.20 eV, respectively). The W-pattern distortion, not considered by Zhang et al., is as effective as the V-pattern distortion in opening a band gap at the Fermi level. The band gap calculated for the W-pattern

(27) Dronskowski, R.; Blöchl, P. E. *J. Phys. Chem.* **1993**, *97*, 8617−8624.

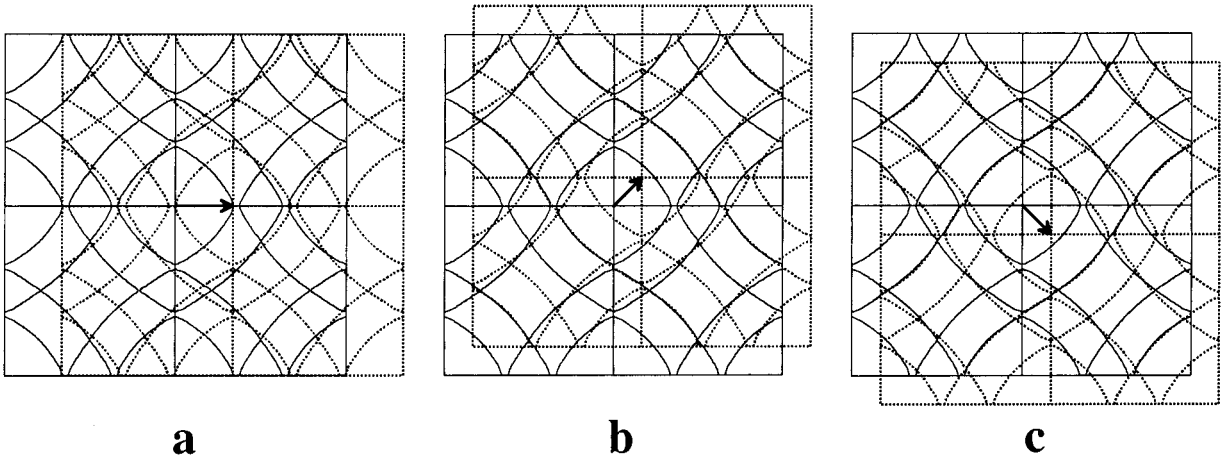

Figure 9. Fermi surface superposition for different nesting vectors: (a) 1/3**a***; (b) 1/6(**a*** + **b***); (c) 1/6(**a*** − **b***).

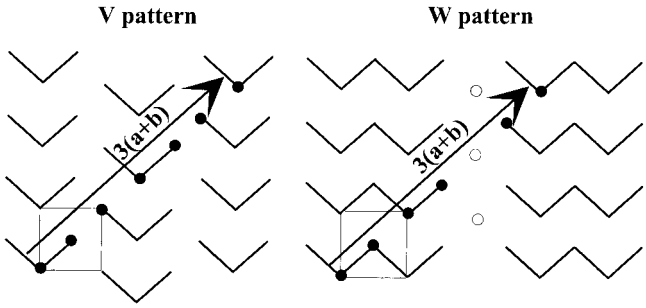

Figure 10. Schematic view of the V and W patterns observed in the Te layers of the incommensurate $K_{1/3}Ba_{2/3}AgTe_2$. The projection of the average cell is given in gray and the superstructure compatible with the nesting vector is shown with arrows along the diagonal directions.

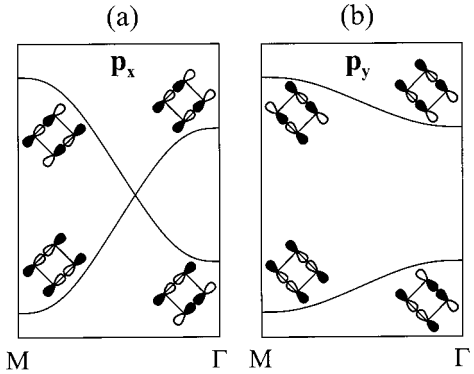

Figure 11. Qualitative dispersion relations of the in-plane Te p orbitals bands along the Γ−*M* direction: (a) Te p_x orbitals; (b)Te p_y orbitals.

distortion (i.e., 0.20 eV) is not too far from 0.06 eV deduced from conductivity measurements.[8]

To find the major orbital character contributing to the bands, partial electron density plots were calculated on the plane of a Te-layer by using the band orbitals in four different energy regions. These are shown in Figures 12b and 13b. The partial density plots reveal that the distortions of models 2 and 3 group the Te p_x/p_y orbital bands into four energy regions; a group of antibonding bands above the band gap, two groups of largely nonbonding bands immediately below the band gap, and a group of bonding bands lying below the nonbonding bands. The nearest neighbor Te atoms within each V- or W-pattern are bonding in the bonding bands and antibonding in the antibonding bands. In the nonbonding bands, there exists a weak bonding between the Te atoms of the adjacent patterns. These observations are in agreement with the findings of Zhang et al. based on orbital interaction analysis.[8]

3.3. Stabilization Associated with Distortion. Let us now examine the total electronic energies of the distorted structures (models 2 and 3) with respect to that of the average structure (model 1). Since the unit cell of model 2 or 3 is 3 times larger than that of model 1, we compare the total electronic energies of the three models based on the tripled unit cell. Figure 14 shows the total electronic energies of models 2 and 3, with respect to that of model 1, as a function of the number of electrons in the unit cell. When all the levels up to the Fermi level are occupied, models 2 and 3 are more stable than model 1, and model 2 is more stable than model 3. This is consistent with the experimental findings that both V- and W-pattern distortions occur in $K_{1/3}Ba_{2/3}AgTe_2$, and that the V-pattern domains are slightly larger than W-pattern domains.

To probe the driving force for the structure distortion in $K_{1/3}Ba_{2/3}AgTe_2$, we examine the total energies of models 2 and 3 calculated as a function of the number of electrons in the unit cell. Figure 14 shows that the stabilization arising from the AgTe-layers (i.e., that contributed by the Te s and Ag d orbital bands) is not significant. When the Te p orbital bonding bands are filled, there results a significant amount of stabilization (between 30% and 50% of the total stabilization). Then, the stabilization increases gradually as the nonbonding Te p orbital bands are filled. A significant increase in stabilization energy occurs when the Te p orbital nonbonding bands near the Fermi level are filled. Thus, the V- and W-pattern distortions bring about stabilization not only from the occupied bands around the Fermi level but also from bonding bands lying well below the Fermi level. It is interesting to note that, up to now, no evidence of the metallic state at high temperature has been given for $K_{1/3}Ba_{2/3}AgTe_2$. This supports the idea that the stabilization of the bands near the Fermi level cannot be the main cause for the distortion.

3.4. Discussion. From the facts that the distortions of models 2 and 3 open a band gap at the Fermi level, and that there occurs a sharp stabilization when filling the Te p orbital nonbonding bands near the Fermi level, one might suggest that the incommensurately distorted structure of $K_{1/3}Ba_{2/3}AgTe_2$ is a consequence of the CDW instability associated with the nesting vectors $\mathbf{k}_1$ and $\mathbf{k}_2$. However, this suggestion is inconsistent with two observations. One is that modulation vector **q** found for $K_{1/3}Ba_{2/3}AgTe_2$ is quite different than the nesting vector $\mathbf{k}_1$ or $\mathbf{k}_2$ ($\mathbf{q} = 0.3248\mathbf{a}^* + 0.2538\mathbf{c}^*$). The other is that the Te p orbital bonding bands lying well below the Fermi level also contribute

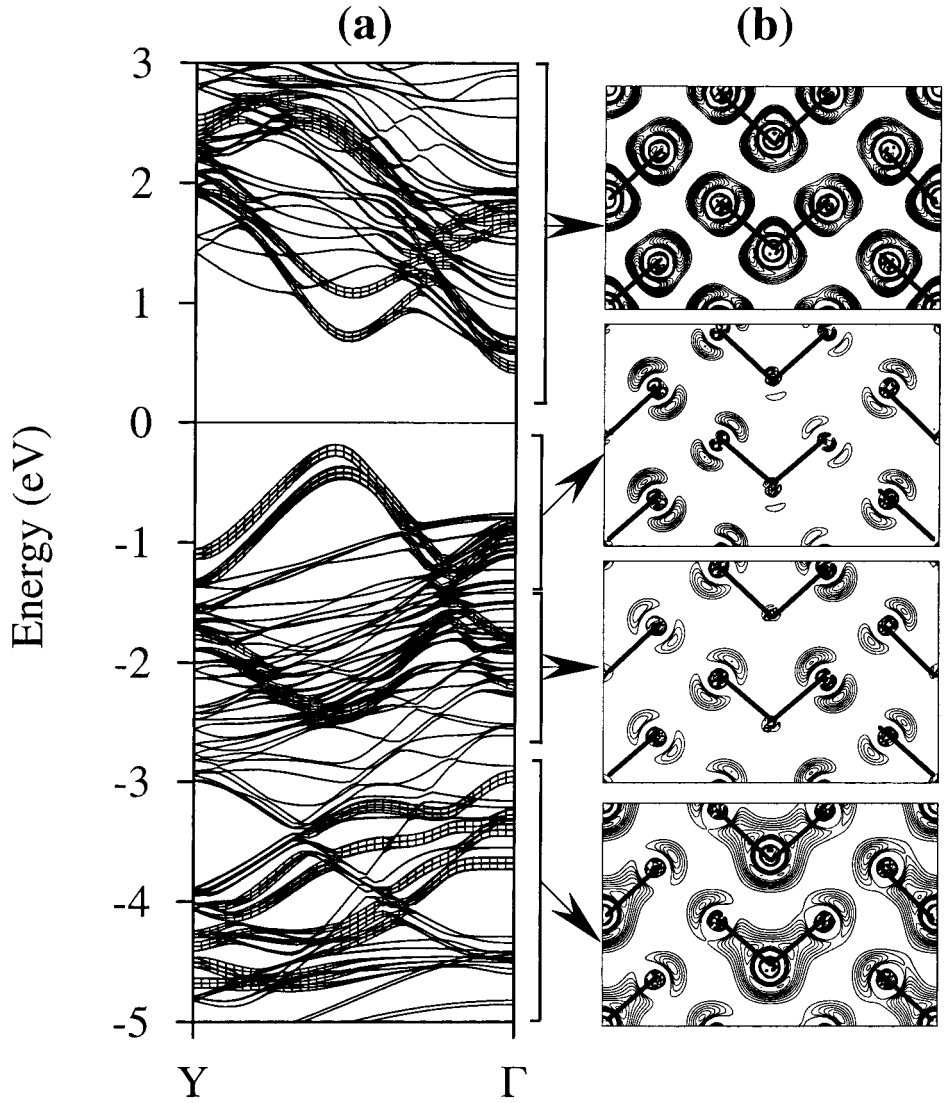

Figure 12. Electronic band structure calculated for the distorted structure of model 2 (V pattern distortion): (a) dispersion relations, where the Te in-plane p orbitals are visualized with a "fat band" representation; (b) partial density plots calculated for the four different energy regions.

significantly to the stabilization so that the distortion can be regarded as a second-order Peierls distortion.[28]

The nesting vector $\mathbf{k}_3 = \mathbf{a}^*/3$ of the ideal Fermi surface is similar to the in-plane component of the modulation vector **q** (i.e., 0.3248 **a***). However, the vector $\boldsymbol{k}_3$ results from the use of the simplifying approximation such as the simple Hückel method. When overlap integrals and nonnearest-neighbor interactions are included in electronic structure calculations, the resulting Fermi surface of the average structure has a sinusoidal warping so that the nesting vector of the true Fermi surface deviates from $\mathbf{k}_3$ and becomes $\mathbf{k}_1$ or $\mathbf{k}_2$. Thus the more accurate nesting vectors of the Fermi surface calculated for the average structure are $\mathbf{k}_1$ and $\mathbf{k}_2$ and these vectors correctly predict the V- and W-pattern distortions observed experimentally. In other words, the Fermi surface nesting vectors of the average structure do predict the Te−Te bonding scheme in the modulated structure but do not predict the modulation vector of the distorted structure.

In the present case, the concept of "hidden" nesting vector, first introduced by Canadell and Whangbo,[29] can be used to interpret the in-plane component of **q** as it has been done for example for the Magnéli phases Mo_4O_{11}.[29] This in-plane component of the modulation vector **q** found for the incommensurately distorted structure of $K_{1/3}Ba_{2/3}AgTe_2$ is related to how the V- and W-patterns of Te atoms are distributed in the Te-layers. Certainly, this distribution is influenced not only by the electronic energy gain resulting from the distortion but also by the lattice strain energy opposing the distortion. So the best way to interpret the in-plane component of **q** is to consider that the distortion leads to the smaller supercell (the larger modulation vector) having a 3-fold superstructure along the both diagonal directions.

The out-of-plane component of the modulation vector **q** (i.e., 0.2538**c*** in a quadratic-like cell representation) should be related to how the sequence of the V- and W-patterns varies along the stacking direction. The modulation along this direction is most probably caused by purely geometrical reasons and it appears that the **c*** component of the **q** wave vector is such that the probability of finding two consecutive V- (or two consecutive W-) patterns is minimal.

When a CDW formation is mainly determined by the stabilization of the occupied bands around the Fermi level, the modulation vector of the distorted structure is correctly predicted by the nesting vector of the Fermi surface calculated for the

(28) Whangbo, M.-H. In *Crystal Chemistry and Properties of Materials with Quasi-One-Dimensional Structures*; Rouxel, J., Ed.; Reidel: Dordrecht, 1986; p 205.
(29) Canadell, E.; Whangbo, M.-H. *Chem. Rev.* **1991**, *91*, 965−1034.

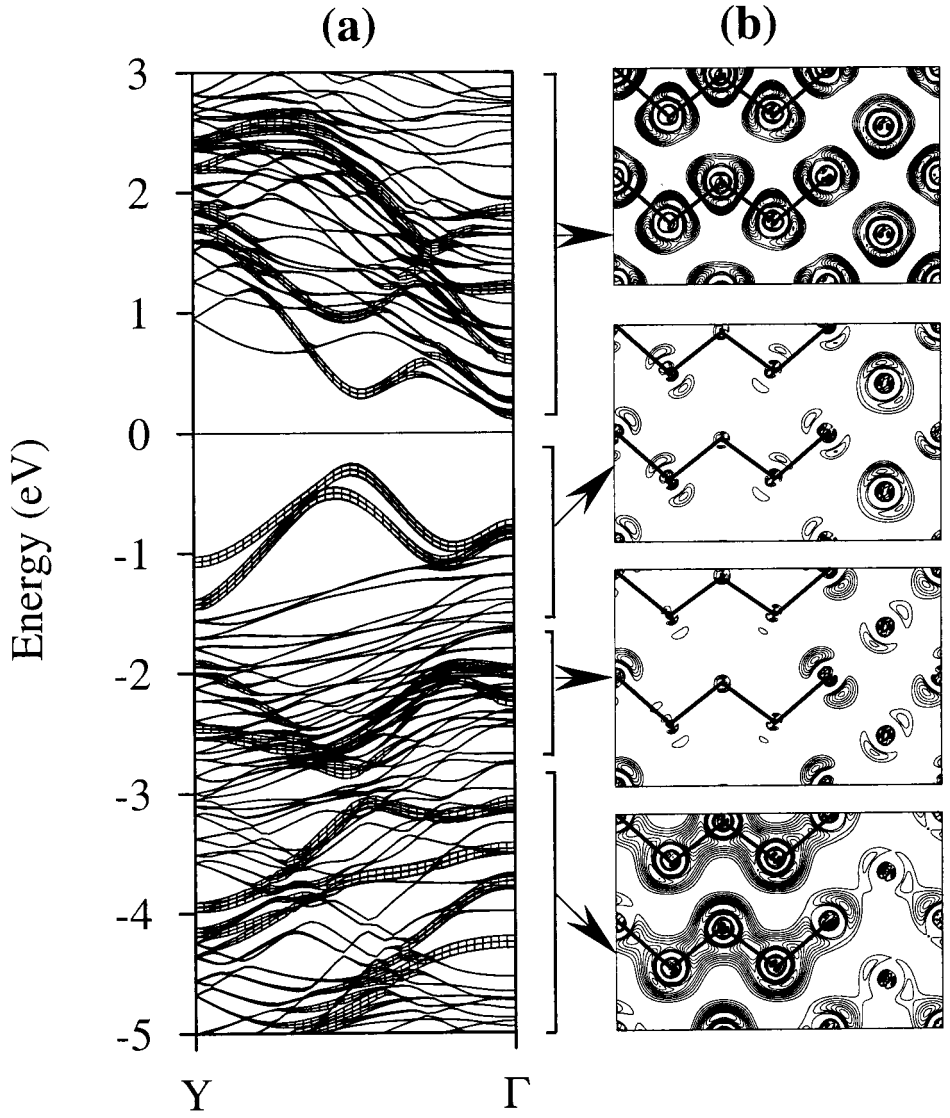

Figure 13. Electronic band structure calculated for the distorted structure of model 3 (W pattern distortion): (a) dispersion relations, where the Te in-plane p orbitals are visualized with a "fat band" representation; (b) partial density plots calculated for the four different energy regions.

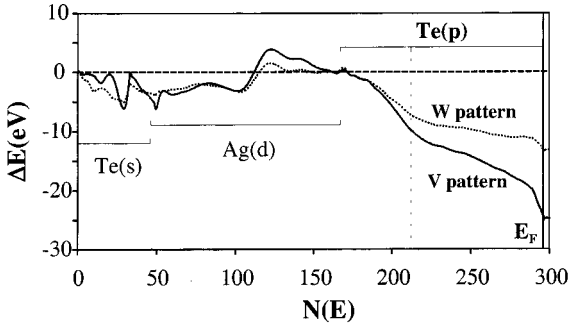

Figure 14. Total energies of the distorted structures of models 2 and 3 with respect to that of the average structure of model 1 calculated as a function of the number of electrons in a tripled unit cell.

corresponding undistorted structure.[29,30] As shown above, the energy stabilization associated with the occurrence of V- and W-patterns is not dominated by the energy change associated with the energy bands in the region of the Fermi level. It should be noted[31] that a number of metallic systems exhibit structural modulations unrelated to the nesting of the Fermi surfaces calculated for their unmodulated structures. Such cases occur as long as the modulation leads to a large enough stabilization in the occupied energy levels lying well below the Fermi level.[31] In the present case, a second-order Peierls distortion could explain why the modulation vector **q** cannot be completely determine from the analysis of the Fermi surface.

4. Concluding Remarks

The determination of the incommensurate superstructure of the square Te net, reported here, reveals additional significant features not detected earlier. The net is comprised of not only regions of V-shaped Te_3 anions arranged in a noncentrosymmetric fashion but also of a region of W-shaped Te_5 separated with Te anions. The Te-net structure then can be characterized as an aperiodic wave of different polytelluride anions propagating along the *b* axis. In agreement with experiment, our band structure calculations show that the distorted structures of V-pattern (model 2) and W-pattern (model 3) are more stable

(30) *Low-Dimensional Electronic Properties of Molybdenum Bronzes and Oxides*; Schlenker, C., Ed.; Kluwer: Dordrecht, The Netherlands, 1989.

(31) Whangbo, M.-H.; Seo, D.-K.; Canadell, E. In *Physics and chemistry of low-dimensional inorganic conductors*; Schlenker, C., Greenblatt, M., Dumas, J., Van Smaalen, S., Eds.; Plenum: New York, 1996; p 285. (b) Whangbo, M.-H.; Canadell, E. *J. Am. Chem. Soc*. **1992**, *114*, 9587−9600.

than the average structure (model 1), and that the V-pattern distortion leads to a slightly larger stabilization than does the W-pattern distortion. The nesting vectors of the Fermi surface calculated for the average structure are consistent with the occurrence of the V- and W-pattern distortions in the Te-layers of $K_{1/3}Ba_{2/3}AgTe_2$, but they are quite different than the in-plane component of the observed modulation vector of the incommensurately distorted structure. This is so because the stabilization energy associated with the distortion is not dominated by the energy lowering of the occupied band levels near the Fermi level.

It is worth noticing that not only the Te_5 structural motif is unprecedented, but essentially two different Te_x anions occur in the same plane. This remarkable discovery implies that the factors giving rise to the particular aperiodic structures in Te-square nets are subtle and begs for the structural determination of additional such structures of related compounds as in $KCuCeTe_4$ and $LnTe_3$, for example.

Acknowledgment. Work at North Carolina State University was supported by the U.S. Department of Energy, Office of Basic Sciences, Division of Materials Sciences, under Grant DE-FG05-86ER45259. Work at Institute of Physics was supported by the Grant Agency of the Czech Republic (202/96/0085). Financial support from the National Science Foundation (Grant DMR-9817287) is gratefully acknowledged.

IC991457G